An IEEE Societies and Technical Councils Publication
IEEE Data Descriptions

Received 30 September 2025; revised 20 February 2026; accepted 21 February 2026; Date of publication 25 February 2026; date of current version 18 March 2026.

Digital Object Identifier 10.1109/IEEEDATA.2026.3668223

Descriptor: *Digital Dataset of Animal Tissues for Macroscopic Pathology in Cancer: Image and Ultrasound Data (DATP-IU)*

FABRIZIA AULETTA [1] (MEMBER, IEEE), MARTON C. MEZEI [1], ILARIA BENEDETTI [1] (GRADUATE STUDENT MEMBER, IEEE), GIACOMO ROSSI [2], ALESSANDRA GAVAZZA [2], AND CALOGERO M. ODDO [1,3] (SENIOR MEMBER, IEEE)

[1]The BioRobotics Institute and Department of Excellence in Robotics and AI, Sant'Anna School of Advanced Studies, 56127 Pisa, Italy
[2]School of Biosciences and Veterinary Medicine, University of Camerino, 62032 Camerino, Italy
[3]Interdisciplinary Research Center Health Science, Sant'Anna School of Advanced Studies, 56127 Pisa, Italy

CORRESPONDING AUTHOR: Fabrizia Auletta and Calogero M. Oddo (e-mail: Fabrizia.Auletta@santannapisa.it; Calogero.Oddo@santannapisa.it).

ABSTRACT Macroscopic descriptions in anatomic pathology play a crucial role in the evaluation of tissue samples and in diagnosis and treatment decisions of patients. This applies to biological specimens in both animal and human oncology. The presented DATP-IU dataset aims to serve as a pioneering effort, starting with animal samples, to create a digital atlas of histopathological tissue specimens at the macroscopic level, enriched with quantitative sensory data. The image and ultrasound data were obtained from formalin-fixed histological animal tissues of varying sizes, types, and origins. The data were analyzed using a rotary-stage coordinate system and compared with manual caliper measurements of the same calibration pattern. The average Z absolute error is 1.02%, and sub-millimeter accuracy is maintained across all camera distances. The automatic regulation of yaw angles via a LabVIEW routine enhanced both accuracy and repeatability by eliminating manual errors and ensuring consistent angular adjustments. The presented DATP-IU dataset offers an innovative approach to making pathology assessments more accurate, reproducible, and accessible.

IEEE SOCIETY/COUNCIL IEEE EMBS; IEEE Sensors Council

DATA TYPE/LOCATION Images, Timeseries; Camerino, Italy

DATA DOI/PID 10.21227/2v1g-ab70

INDEX TERMS Digital-atlas, ex-vivo tissue scanning, image-based pathology, macroscopic imaging, ultrasound data.

BACKGROUND

Like in human medicine, macroscopic (or gross) descriptions in veterinary pathology play a critical role in the evaluation of tissue samples and in the diagnosis and treatment decisions of animals [1]. The macroscopic description process involves the visual examination of excised tissues or organs, focusing on characteristics that can be observed with the naked eye, such as size, shape, color, and texture. This helps to identify visible abnormalities, such as growths, organ enlargement, and lesions, and supports the diagnosis of conditions such as cancer, infections, and degenerative diseases [2]. Macroscopic descriptions can also help veterinarians and specialists to decide on treatments, such as additional surgery, chemotherapy, or other follow-up care. For example, in veterinary oncology, the gross appearance of a tumor—its margins, texture, and whether it invades nearby tissues—can suggest the type of cancer and its progression, helping to formulate a preliminary diagnosis before microscopic examination [3].

At the same time, macroscopic descriptions in veterinary pathology are important in the research setting. In fact, veterinary pathology often serves as a basis for animal models that mimic human diseases [4], [5]. For example, macroscopic descriptions of tumors or other pathologies in animals (such as dogs and mice) can provide insight into similar diseases in humans [6]. Similarly, macroscopic assessments are used, in both human and veterinary research, to assess the efficacy of new drugs or treatments. These findings, documented through macroscopic descriptions, are a crucial step before microscopic examination and are important in both preclinical animal studies and veterinary trials [7], [8]. In traditional pathology, after the macroscopic assessment, the excised tissues are typically reduced to smaller cuts, embedded in paraffin blocks, and sliced for microscopic examination [9]. This process, though necessary for detailed histological analysis, inherently destroys the original macroscopic context and structural integrity of the tissue.

Additionally, macroscopic assessments are often subjective, relying heavily on the expertise and sensory sensitivity of the pathologist, which can lead to variability in reporting. In this context, the presented DATP-IU dataset aims to serve as a pioneering effort to create a digital atlas of histopathological tissue specimens at the macroscopic level, enriched with quantitative sensory data. By preserving the macroscopic appearance in a digital format and supplementing it with objective measurements, this dataset offers an innovative approach to making pathology assessments more accurate, reproducible, and accessible.

The dataset includes 200 color images, 200 depth images, 200 transformation matrices, and single-channel ultrasound pulse-echo responses for 54 excised tissues, for a total of 32 788 data points. The color images provided in the dataset capture the visible features of the excised tissues, such as size, shape, texture, and color, offering a traditional macroscopic view of the tissue. The depth images introduce a 3-D component to the digital twin, allowing a more detailed analysis of the tissue's volume and surface irregularities. Transformation matrices provide spatial and geometric information about the alignment and orientation of tissue specimens during imaging [10], [11]. Ultrasound data capture the acoustic properties of tissues, providing sensory information about specimen density, stiffness, and internal composition [12], [13].

COLLECTION METHODS AND DESIGN

The dataset was collected in a collaboration between bioengineering researchers of the BioRobotics Institute of Sant'Anna School of Advanced Studies (Pisa, Italy) and researchers of the School of Biosciences and Veterinary Medicine at the University of Camerino (Italy) between May 2024 and December 2024. The collaboration led to the creation of a tissue bank of 54 excised tissues, thus favoring the gathering of extensive data, combining multiple layers of information, from color and depth imaging to single-channel, high-frequency ultrasound response, to microscopic analysis results.

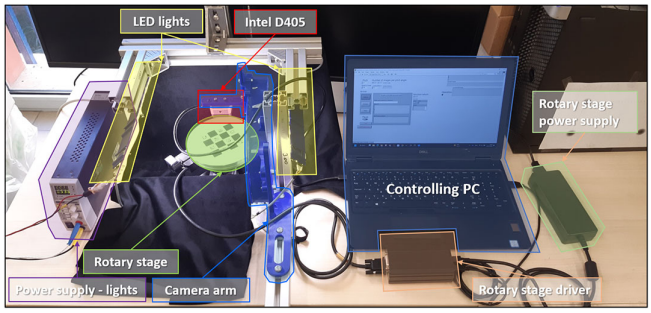

FIG. 1. Scanner platform components: the vision system (Intel Realsense D405 and the adjustable camera arm), the rotary stage system (the rotary stage, the driver, and the power supply), the illumination system (LED strips and power supply), and the controlling PC.

The tissue specimens were obtained from animal patients who underwent routine veterinary procedures, specifically by surgical excision of nodules and other lesions between May 2024 and December 2024. Subsequent to excision, the tissue specimens were promptly placed in 10% neutral buffered formalin [14], [15]. The fixation process is the standard procedure that ensures the preservation of the structural integrity of the tissue and the prevention of tissue degradation, thereby enabling an accurate microscopic examination at a later stage [16]. Each specimen was tagged with a three-digit number to ensure accurate identification throughout subsequent analyses [17], [18] and divided into two halves to obtain two sub-specimens as symmetrical as possible. One sub-specimen was designated for the primary histological assessment, while the remaining half was reserved for further research investigations. For the first half, the results of the histological assessment were documented for each scanned slide and subsequently validated by the pathologist. The remaining sub-specimen was utilized to compile the *dataset* (image and ultrasound) presented in the following sections. In each section, the presentation begins with the image data and then progresses to the ultrasound data.

Image Data Collection

The image data were collected with the custom-made semi-automatic scanner platform shown in Fig. 1. The platform enabled the capture of both RGB-D images and point clouds, with known camera positions, of potentially n = 5.184.000 views of any object placed on the platform. This was achieved through the integration of an RGB-D camera (Intel RealSense D405, USA), a rotary stage (Standa 8MR190-2-28, Lithuania), an light emitting diode (LED) lighting system, and a 3-D-printed adjustable polylactic acid (PLA) camera stand. The semi-automatic scanner platform was controlled by a LabVIEW application integrating the XiLab LabVIEW library (XIMC SDK 2.13.3) for the rotary stage and the Intel RealSense

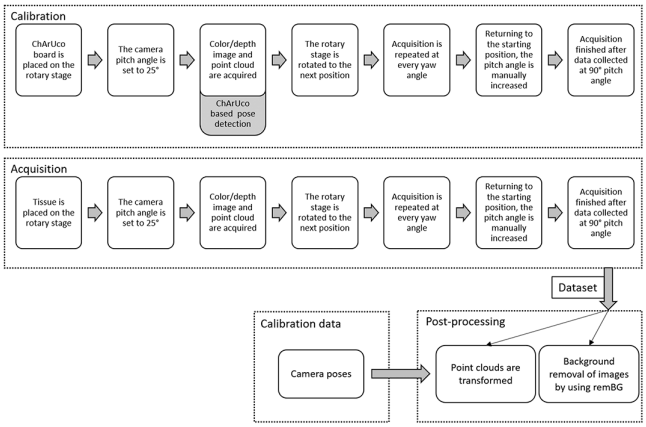

FIG. 2. Workflow of the image dataset collection. The *calibration phase* comprises the placement of the ChArUco board on the rotary stage. This is followed by the dataset *acquisition phase*, performed for each tissue specimen. Finally, in the *post-processing phase*, the backgrounds can be removed, and the collected point clouds can be transformed into the reference coordinate system through the transformation matrices computed during the *calibration phase*.

SDK 2.0 (ver 2.54.2.5684) Python library for the RGB-D camera. Client-server communication was established between the LabVIEW (2019 SP1 32-bit) and Python (3.8.18) environments to coordinate object positioning and data collection.

The image collection process, detailed in Fig. 2, comprised three phases: 1) the acquisition phase; 2) the calibration phase; and, optionally; and 3) the post-processing phase. The *acquisition phase* corresponded to the actual image data collection; that is, RGB images, depth images, and point clouds from multiple points of view. Precisely, six viewing pitch angles N_{pitch} were selected within the range of 25°–90°. The yaw angles were automatically regulated by the rotary stage, which rotated from 0° to 360° at equal intervals of N_{interval} degrees between each adjacent view. Table I reports the number N_{images} of images taken at each viewing pitch angle and the degrees of the yaw angle intervals. The tissue specimens scanned had an inherent variability in terms of size and shape. To ensure the precise collection of image data, the distance between the camera and the plane, on which the specimens were positioned, was calibrated accordingly. The camera distance, measured from the center of the rotary stage, was adjusted between 70, 90, and 130 mm. For smaller specimens, the camera was positioned in closer proximity to the object (i.e., 70 mm) and maintained at this distance throughout the image data collection process.

However, alterations to the camera distance impacted the sensitivity of the depth images, particularly given that the 70 and 90 mm distances approached the limits of the sensing capabilities of the RGB-D camera. To maintain coherent depth information, the resolution of the depth images was reduced from 1280 × 720, which was the resolution used for the 130 mm distance, to 848 × 480 for the 90 mm distance, and to 640 × 320 for the 70 mm distance. The coherent

TABLE I. Number of Images (N_{images}) and Yaw Angle Intervals Amplitudes (N_{interval}) for Each Selected Viewing Pitch Angle (N_{pitch})

N_{pitch}	N_{interval}	N_{images}
25°	12°	30
35°	14.4°	25
45°	18°	20
60°	27.7°	13
75°	45°	8
90°	90°	4

modulation of resolution and proximity of the camera to the specimen ensured the preservation of tissue details and the provision of well-defined features, which are crucial for numerous 3-D reconstruction techniques [10], [11], [19], [20], [21].

To facilitate the use of the presented DATP-IU dataset for tissue specimen 3-D reconstruction, the *calibration phase* involved the computation of the transformation matrices between the camera-centered reference frame and the reference frame centered on the ChArUco board's origin at each viewing angle. The precise calibration of the scanner platform entailed determining the transformation matrices between each position of the camera and the ChArUco board's origin. The calibration phase was nearly identical to the general scanning process except for the object placed on the rotary stage (see Fig. 2). During the calibration process, a ChArUco board was placed on the rotary stage. A Python script, integrating OpenCV library functionalities,[1] detected the ChArUco markers and calculated the transformation matrices for all camera positions. These matrices can subsequently be applied to specify the camera positions in the general scanning process.

Ultrasound Data Collection

Similarly to the image data, the ultrasound data were collected with the custom-assembled ultrasonic platform in Fig. 3. The platform consisted of three micrometric manual translation stages (Standa 085082, Lithuania), a single channel transmitter/receiver device (Lecouer Électronique US-KEY, France), and a needle-shaped ultrasonic probe (Sonomed SPW16, Poland). The separate elements of the platform are combined through the PLA 3-D printed substrate.

The ultrasound signal was generated and received via the US-KEY device, powered via a 5 V DC USB port. The transmitter within the device can generate user-programmable pulses. For signal amplification, a low-noise preamplifier was combined with a variable gain amplifier, providing a gain range from 0 to 80 dB. The ultrasound signals were digitized using a 12-bit analog-to-digital converter, which operated at a sampling frequency of 80 MHz. The signal

[1] https://docs.opencv.org/4.x/d0/d3c/classcv_1_1aruco_1_1CharucoBoard.html

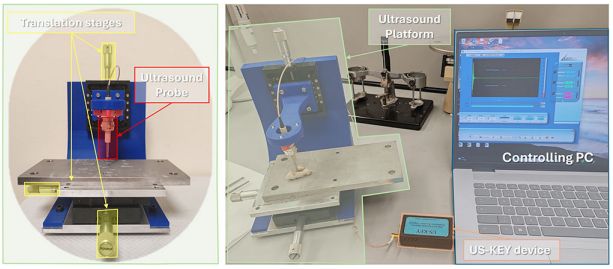

FIG. 3. Ultrasound system components and data collection set-up: the manual platform with three micrometric translation stages, the ultrasound probe, and the stainless-steel plate. The probe is connected to the US-KEY device, controlled by the PC via a user interface.

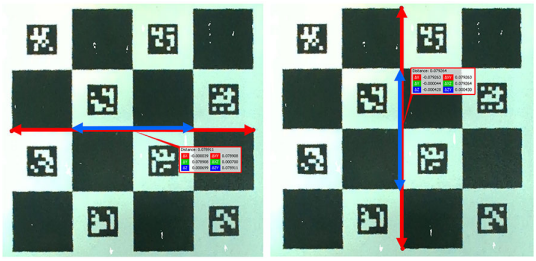

FIG. 4. Dimensions (height and width) of the ChArUco board, measured on the point cloud reconstruction at 130 mm camera distance (red arrows) and at 70 and 90 mm camera distances (blue arrows).

was collected in A-scan mode, which made it easy to detect defects, determine their position, and evaluate their reflectivity. All acquisitions were conducted in HF 80 MHz "full-wave mode." The ultrasound data collection system was controlled by the US-KEY DLL application (version 2.0.12.0, Lecouer Électronique, France).

The ultrasonic needle probe operated at a center frequency of 16 MHz and a fractional bandwidth of 0.25 at −6 dB, in pulse-echo mode [22]. The probe had an external diameter of 3 mm and an active piezoelectric element of 2 mm.

Two of the moving stages, orthogonally mounted beneath a supporting stainless-steel plate, enabled the tissue specimen to be moved in two directions (X-axis and Y-axis). The third stage, mounted vertically (Z-axis), held the ultrasonic probe through a 3-D-printed structure, enabling adjustable vertical positioning at varying distances from the specimen. Each stage had a 25 mm range of movement, covering a total volume of $25 \times 25 \times 25$ mm^3. The specimen was positioned on the stainless-steel plate, which both enhanced optimal reflection of the ultrasound signal and facilitated sterilization procedures.

A *calibration phase* of the ultrasonic platform was specifically performed to tune, along the Z-axis, the distance between the ultrasonic probe and the stainless-steel plate.

The first step of the process was to establish the "zero distance," defined as the point at which the probe made physical contact with the plate. To this end, the probe was lowered until its piezoelectric element contacted the plate. Once the position of the probe had been established, the probe was then lifted out of contact using the Z-axis moving *stage*. When a histopathological specimen was placed on the plate in the *acquisition phase*, the probe was lowered once more to touch the tissue.

The distance between the tip of the probe and the plate, then, corresponded to the thickness of the specimen, which can be directly read on the micrometric scale.

VALIDATION AND QUALITY

Image Data Validation

The image data were collected with the Intel RealSense D405 depth camera, having a Z-accuracy below ±2% for camera distance from the object below 500 mm while achieving submillimeter accuracy at a camera distance of 70 mm [23]. A thorough evaluation of the depth accuracy of the camera was conducted using predefined calibration boards designed for ChArUco marker detection. The depth evaluation process was performed at 70, 90, and 130 mm camera distances. The pitch angles of the technical validation acquisitions were identical to those of the standard data acquisition procedures, which were 25°, 35°, 45°, 60°, 75°, and 90°. For each pitch angle, six acquisitions were taken from different yaw angles, resulting in a total of 36 width and 36 height measurements for each camera distance, summing to 216 measurements overall. CloudCompare 2.13 [GPL software] point cloud handling software was employed to measure the height and width of the ChArUco board pattern in the captured point clouds (see Fig. 4 for an example). These measurements were compared with caliper measurements of the same calibration pattern. The results show that the average Z absolute error is well below 2%, and the submillimeter accuracy is maintained across all camera distances (see Table II).

TABLE II. Comparison of Real and Reconstructed Dimensions at Various Camera Distances

	Camera Distances		
	130 mm	90 mm	70 mm
Real board dimension (mm)	79.5	39.75	39.75
Reconstructed dimension (mm)	78.9 ± 0.5	39.7 ± 0.25	39.6 ± 0.31
Average Z signed error (%)	0.592	0.025	0.104
Average Z absolute error (%)	0.745	0.062	0.261

Furthermore, the mechanical structure of the scanner platform ensured precise geometric alignment, with the optical axes of all views intersecting at the center of the rotary stage. The fixed camera position provided stable, uniform image capture, minimizing variability and ensuring consistent data collection. Additionally, the automatic regulation of yaw angles via a LabVIEW routine enhanced both accuracy and repeatability by eliminating manual errors and ensuring consistent angular adjustments. Together, these elements contributed to a robust and reliable acquisition process for comprehensive and accurate imaging.

Ultrasound Data Validation

Ultrasound data were collected with standardized equipment and methodologies to ensure consistency and repeatability.

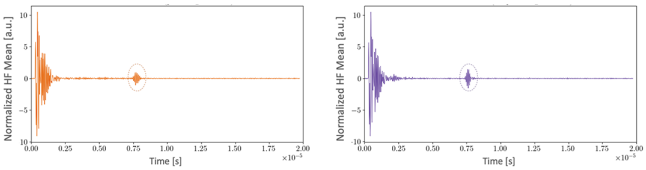

FIG. 5. Comparison of (a) "pathological area" and (b) "not pathological area" of the ultrasound data collected on a tissue sample of *subcutaneous mast cell tumors*. The variation in the amplitude of the reflection peak is highlighted by the dotted circle.

A high-frequency probe at 16 MHz was utilized for data collection, which allowed for greater resolution and more precise measurement of the target tissues. The quality of collected data was evaluated based on the clear discernibility of a reflection peak in the received ultrasound signal, a crucial indicator for tissue characterization in accordance with the instrumentation. In certain instances, a more discernible reflection peak was observed, which could be attributed to the specific acoustic properties of the area evaluated (see Fig. 5 for an example). For these reasons, the subsequent labeling of the ultrasound data point was conducted in close collaboration with expert researchers, thus ensuring the accuracy and reliability of the interpretations. This interdisciplinary approach permitted a comprehensive validation of the collected data, aligning the results with established medical expertise and ensuring the robustness of the labeling process. In instances where it was not feasible to visualize the pathological area with the assistance of the medical team, the label "N/A" was included in the label section to prevent any potential misinterpretations in later uses of the dataset.

RECORDS AND STORAGE

All data records were deposited in the IEEE DataPort repository under a DOI number of 10.21227/2v1g-ab70. The dataset is intended for non-commercial purposes under FAIR use principles. The image and ultrasound data were obtained from formalin-fixed histological animal tissues of varying sizes, types, and origins, carefully washed before their digitization. Details regarding the gender, age, type of specimen material, and diagnosis can be found in the *sample_metadata.json* file. The dataset is diverse, encompassing a wide range of tissue specimens. The dataset is organized such that each tissue specimen is assigned a dedicated folder, identified by a unique, pseudonymous ID. Within these folders, two distinct types of data are provided for every specimen: image data from the "ScannerPlatform" folder and ultrasound data from the "UltrasoundPlatform" folder. A representation of the dataset folder structure is provided in Fig. 6.

Image Data

A total of 54 tissue specimens were scanned using the scanner platform. We collected 14 specimens at a 70 mm camera distance, 28 specimens at a 90 mm camera distance, and 16 specimens at a 130 mm camera distance. For each

```
.
└── SampleID
    ├── SampleID_metadata.json
    ├── ScannerPlatform
    │   ├── SampleID_bottom
    │   │   ├── CAMERA_poses
    │   │   │   ├── Transformation_matrix_1.json
    │   │   │   ├── (...)
    │   │   ├── IMG_color
    │   │   │   ├── IMG_color_original
    │   │   │   │   ├── IMG_color_original_1.png
    │   │   │   │   ├── (...)
    │   │   │   ├── IMG_color_segmented
    │   │   │   │   ├── IMG_color_segmented_1.png
    │   │   │   │   ├── (...)
    │   │   │   └── type_metadata.json
    │   │   ├── IMG_depth
    │   │   │   ├── IMG_depth_original
    │   │   │   │   ├── IMG_depth_original_1.png
    │   │   │   │   ├── (...)
    │   │   │   ├── IMG_depth_segmented
    │   │   │   │   ├── IMG_depth_segmented_1.png
    │   │   │   │   ├── (...)
    │   │   │   └── type_metadata.json
    │   │   ├── PointClouds
    │   │   │   ├── Pointcloud_1.ply
    │   │   │   ├── (...)
    │   │   └── hemisphere_metadata.json
    │   ├── SampleID_top
    │   │   ├── (...)
    │   └── scanner_metadata.json
    └── UltrasoundPlatform
        ├── IMG_pictures
        │   ├── SampleID_1.jpg
        │   ├── (...)
        ├── US_signals
        │   ├── SampleID_1_Ascan.csv
        │   ├── (...)
        └── ultrasound_metadata.json
```

FIG. 6. Example of dataset internal organization, "SampleID" represents any randomly generated ID of each sample in the dataset. Note that the "SampleID_top" and "SampleID_bottom" internal structures coincide, so one is omitted for the sake of presentation.

sample, two opposite stable placement orientations were identified, with the constraint that the contact surfaces of the two orientations were on opposite sides of the tissue to ensure a comprehensive camera view coverage of the specimen. A top and a bottom side were designated from the two orientations. For both hemispheres, a dataset of 100 acquisitions was collected, starting with the top side. After conducting the measurements, the specimen was manually re-placed to acquire the dataset for the bottom hemisphere. In each "ScannerPlatform" folder, a *scanner_metadata.json* file stores the measurement parameters and two folders, one for each hemisphere. In each hemisphere folder, the image data are distributed in the following subfolders.

1) "CAMERA_poses" contains the transformation matrices, calculated during calibration, in JSON format.
2) "IMG_color_original" contains raw color (RGB) images in PNG format at 1280×720 resolution.
3) "IMG_color_segmented" contains AI-segmented color images (1280×720 resolution), in PNG format.
4) "IMG_depth_original" contains raw depth images in PNG format with either 1280×720, 848×480, or 640×320 resolution, depending on 130, 90, and 70 mm camera distance from the tissue specimen, respectively.
5) "IMG_depth_segmented" contains AI-segmented depth images (either 1280×720, 848×480, or 640×320 resolution).
6) "PointClouds" contains the point clouds, transformed by the transformation matrices, in PLY format.

Finally, *hemisphere_metadata.json* and *type_metadata.json* store hemisphere-specific and type-specific metadata, respectively, in JSON format.

TABLE III. Metadata Attributes and Their Corresponding Descriptions and Sources for Tissue SpecimensAQ5

Annotation	Description	Metadata Level
Tissue ID	Unique identifier assigned to each tissue specimen	Sample
Species	Species of the patient from which the tissue was obtained	Sample
Gender	Gender of the patient from which the sample was collected	Sample
Age	Age of the patient at the time of sample collection, expressed in years	Sample
Tissue (sample) [additional info]	Type of biological material in the sample (e.g., skin, liver)	Sample
Diagnosis [additional info]	Medical diagnosis associated with the tissue	Sample
Medical history	Relevant medical history of the individual	Sample
Fixation method	Method used to preserve the tissue specimen	Sample
Diagnostic center	Institution where the tissue was diagnosed	Sample
List of scanner-ultrasound pairs	Pairings of scanner and ultrasound data	Sample

Ultrasound Data

A total of 51 tissue specimens were examined using the ultrasonic platform (Fig. 3). In most instances, the reflection peak of the ultrasound signal was clearly discernible. The ultrasound signal provided is the average signal from which background noise has been removed. Each "UltrasoundPlatform" contains an *ultrasound_metadata.json* file that stores the measurement parameters and the following subfolders.

1) "US_signals" contains the ultrasound signal for each data point, in CSV format.
2) "US_pictures" contains the pictures of the analyzed specimen and of the indentation position of the ultrasound probe for each ultrasound signal, in JPEG format.

Connecting the Image and Ultrasound Dataset

A link is provided for 51 specimens between the ultrasound and the image data. Such a connection could be utilized to facilitate further investigations into the acoustic and biomechanical properties of the tissue, while simultaneously integrating these findings with precise 3-D coordinates of the tissue. As mentioned, during each ultrasound measurement, an image of the specimen and its indentation position was captured. By knowing the extrinsic parameters of the camera and identifying the pixel coordinates of the tip of the ultrasound probe, the 3-D coordinates of the indentation position can be calculated.

Data Annotation

The annotation process was conducted both during and after data collection, with pseudo-anonymization to ensure the removal of sensitive information associated with each tissue specimen. Annotations are organized across multiple dictionaries and stored in JSON format within each sample folder, as illustrated in Fig. 6. A detailed explanation of each annotation, along with its location in the **_metadata.json* files, is provided in Tables III–V.

TABLE IV. Metadata Attributes and Their Corresponding Descriptions and Sources for Scanner Data

Annotation	Description	Metadata Level
Collector ID	Identifier of the individual that collected the data	Scanner
Date of acquisition	Date when the data was collected	Scanner
Camera model	Model name of the scanner camera	Scanner
Camera serial	Serial number of the scanner camera	Scanner
Camera distance	Distance of the camera from the sample during image data collection, expressed in millimeters (mm)	Scanner
Camera resolution	Resolution settings of the camera for depth acquisitions	Scanner
Background	Details about the background during image data collection	Scanner
Illumination	Description of the illumination conditions during image data collection	Scanner
Intrinsic matrix	Camera intrinsic parameters used for calibration	Scanner
Distortion matrix	Camera distortion parameters for image correction	Scanner
Tissue hemisphere	Hemisphere of the tissue sample (i.e., top, bottom)	Hemisphere
Exposure time	Exposure time used during image data collection	Hemisphere
Image type	Type of image produced (i.e., color, depth)	Type
Segmentation method	Algorithm used for image segmentation	Type
Number of images	Total number of images collected for the hemishpere-type pair	Type

INSIGHTS AND NOTES

The dataset is organized into folders, each corresponding to a unique tissue specimen identified by a randomly assigned ID. For every tissue specimen, two types of data are provided: image data from the "ScannerPlatform" folder and ultrasound data from the "UltrasoundPlatform" folder. Both data types, along with their associated metadata, are detailed in the "Records and Storage" section. Users have the flexibility to access either platform's data individually or to use the combined dataset. The dataset employs standard file formats, including CSV for tabular data and JPEG for images. These formats were selected for their ease of use and compatibility with a wide range of software tools and programming languages. This guarantees that users can process the data without restrictions on specific software environments.

To our knowledge, there are no similar digital datasets in human or veterinary digital pathology, although microscopic

TABLE V. Metadata Attributes and Their Corresponding Descriptions and Sources for Ultrasound Data

Annotation	Description	Metadata Level
Collector ID	Identifier of the individual that collected the data	Ultrasound
Date of acquisition	Date when the data was collected	Ultrasound
Probe model	Model of the ultrasound probe used	Ultrasound
TX/RX device model	Model of the transmitting/receiving device used in ultrasound imaging	Ultrasound
TX/RX device params	Parameters of the transmitting/receiving device	Ultrasound
Number of data points	Total number of data points recorded in ultrasound data collection	Ultrasound
Data labels—Label	Label for data analysis. The label "pathological area" refers to regions visibly impacted by pathological processes, whereas the label "not pathological area" refers to areas that can be regarded as non-pathological. The label "necrosis area" refers to necrotic regions. The value "N/A" was given in the event of no discernible reflection peak or if it was not possible to assess the pathological status of the point of contact	Ultrasound
Data labels—Height	Thickness of the tissue situated beneath the ultrasonic probe, expressed in millimeters (mm)	Ultrasound
Data labels—Gain	Gain value set on the ultrasound TX/RX device for each acquisition, expressed in decibels (dB)	Ultrasound
Data labels—Filter MHz	Filtering mode set on the ultrasound TX/RX device, expressed megahertz (MHz)	Ultrasound

histopathological slide datasets are becoming increasingly common [24], [25], [26], [27], [28], and a book comprising a collection of photos has recently been published for pathologists and medicine students [29]. The unique dataset presented here can, for example, advance the training of artificial intelligence (AI) methods and the creation of digital twins in anatomic pathology, where a digital twin is defined as a digital replica of a physical object, often enhanced with sensory data that can be accessed in the translational application of the model in the decision-making process. Although digital twins have been widely explored in fields such as engineering and manufacturing, their application to pathology is still in its infancy [30], [31].

In addition, the dataset could be integrated into a broader digital pathology pipeline where macroscopic images, sensory data, and even microscopic data are combined to form an end-to-end diagnostic model. This multi-scale integration would provide a comprehensive view of tissues, combining gross anatomical features with fine histopathological details [11].

SOURCE CODE AND SCRIPTS

Python routines to process and visualize the dataset are freely available on the following repository: https://github.com/Neuro-Robotic-Touch-Laboratory/histologydata. The code is written to work with Python 3.11.5. The *load_dataframe_demo.py* script provides a basic example for loading, selecting, and plotting the data records, making it a good starting point for new users. For more advanced data visualization, the *visualize_data.py* script demonstrates how to generate structured plots from the dataset, providing a more in-depth approach to interacting with the data. To complement the raw data provided, a variety of post-processing techniques can be applied with the intention of enhancing the subsequent analysis and interpretation. The following sections present a discussion of the methods that can be employed to refine and extract meaningful insights from both the image and ultrasound data.

Image Data Post-Processing

While the calibration process ensures the accurate determination of camera positions for precise data collection, an additional post-processing phase can be performed. For example, the dynamic changes in the orientation of the tissue specimens during scanning may pose a challenge in terms of background noise. That is, during the collection of image data of a tissue specimen, the orientation between the specimen and the camera inherently undergoes a continuous change. However, the orientation between the background and the camera remains unaltered between adjacent views, with the exception of instances where the viewing angle is adjusted. Consequently, the relative position of the specimen and its surroundings changes dynamically, which could potentially give rise to complications during 3-D reconstruction processes [10], [21].

To address this challenge, we employed the remBG open-source deep learning segmentation algorithm[2] to eliminate the background. Such an algorithm allowed for the selection of a variety of segmentation models. Based on empirical evidence, the default U2-Net segmentation model demonstrated the most reliable performance in background removal. U2-Net is a deep convolutional neural network pre-trained using a comprehensive image database with the objective of removing backgrounds [32]. Fig. 7 illustrates the different stages of the data processing from the RGB and depth information. Three main steps are highlighted: 1) acquisition of raw data—RGB and depth images—and generating the point cloud; 2) post-processing of the images and point clouds by segmenting the background of the images and transforming the point clouds into a common coordinate system; and 3) identification of the image-pairs of the ultrasound and scanner images. The image-pair finding phase was detailed in the "Connecting the Image and Ultrasound Dataset" section.

Finally, it should be noted that the provided point clouds are not the raw outputs from the cameras themselves. Rather, they have been transformed into the coordinate system of the ChArUco board through the application of the provided transformation matrices, computed in the calibration phase.

[2]https://github.com/danielgatis/rembg

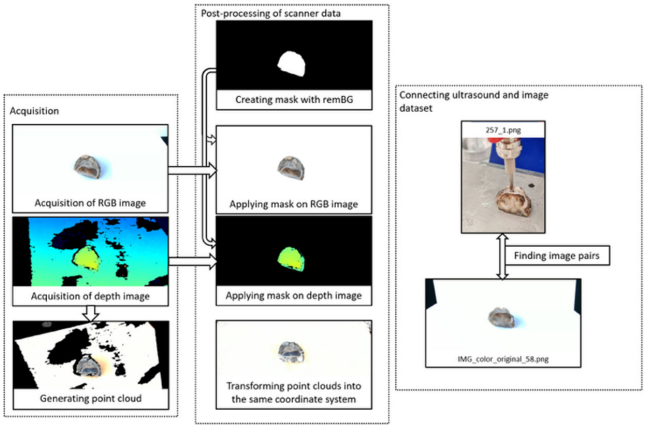

FIG. 7. Data flow of the scanning process. Initially, RGB and depth data are acquired at each camera position, and a point cloud is generated from the depth image. During post-processing, segmentation masks are applied to the RGB and depth images, and the point clouds can be transformed into a common coordinate system using the calibration transformation matrices. Finally, a link between the ultrasound and the image data can be established by identifying the scanner image whose position is closest to the ultrasound image.

In the event that a new camera position detection method is to be tested, the initial step is to reverse-transform the point clouds to their original state using the inverse of the relevant calibration transformation matrix. An example of this process is provided in the published data processing script *process_data.py*.

Ultrasound Data Post-Processing

The calibration phase ensured the correct coupling among the probe, the tissue specimen, and the reflecting surface, thus ensuring an accurate transmission of the ultrasound wave across the different materials. However, the specimens analyzed were fixed ex-vivo specimens, which caused a significant attenuation of the reflection peak.

To address this, the following post-processing phase enables the comparison of point collections on the same specimen and among specimens, even if carried out at different gains. In fact, the gain was empirically adapted among acquisitions and specimens to verify the presence or absence of the reflection peak in areas of non-pathological tissue. Building on this, the normalized signal can be computed as

$$S_{\text{norm}} = S/(V{*}A) = (S_{\text{out}} - 2^{11})/(V{*}10^{\text{G}/20}) \quad (1)$$

where V is the applied voltage, G is the specific gain employed for the data collection, and A is the amplification factor. The signal S considers the electronic digitization of the receiver device; i.e., through the difference between the output signal S_{out} and 2^{11}.

ACKNOWLEDGMENT

The authors would like to thank Domenico Camboni, Lucia Biagini, and Danilo De Bellis for their technical and collaborative support. This research was supported by the project "IMEROS 4.0" funded by RoboIT and the projects "THE—Tuscany Health Ecosystem" (Spoke 8, CUP J13C22000420001) and "ROGER—Robot-assisted Gross Examination of solid tumors" (PNRR-POC-2022-12376137), both funded by the European Union—Next Generation EU through Italian Ministry of University and Research and Italian Ministry of Health, respectively.

Marton C. Mezei and Ilaria Benedetti contributed equally to this article. F.A., M.C.M., and C.M.O. conceived the experiments for image data collection, while F.A., I.B., and C.M.O. conceived the experiments for ultrasound data collection. G.R. and A.G. conducted the histological assessment of the animal tissues and provided the samples, including the related specimen preparation and management tasks and the clinical supervision. M.C.M. and I.B. carried out the experiments, with the operational supervision of F.A.; and F.A. integrated the database and code developed by M.C.M. and I.B. and additionally created the visualization code. C.M.O. is the scientific coordinator of the project. All authors analyzed the results and reviewed and approved the manuscript.

C.M.O. declares patent number EP19704460 on Apparatus for the ex-vivo intraoperative analysis of biological tissue samples. The RoboIT project has the objective to lead to the fundation of a start-up company.

REFERENCES

[1] R. E. Schmidt, "Practical gross pathology," *Seminars in Avian Exotic Pet Med.*, vol. 12, no. 2, pp. 59–61, 2003.
[2] B. Rekhi et al., "Grossing and reporting of a soft tissue tumor specimen in surgical pathology: Rationale, current evidence, and recommendations," *Indian J. Cancer*, vol. 58, no. 1, pp. 17–27, 2021.
[3] O. Gemeinhardt et al., "Comparison of bipolar radiofrequency ablation zones in an in vivo porcine model: Correlation of histology and gross pathological findings," *Clin. Hemorheol. Microcirc.*, vol. 64, no. 3, pp. 491–499, 2017.
[4] D. S. Martin, R. A. Fugmann, R. L. Stolfi, and P. E. Hayworth, "Solid tumor animal model therapeutically predictive for human breast cancer," *Cancer Chemother. Rep. 2*, vol. 5, p. 89, 1975.
[5] F. K. Storm, W. H. Harrison, R. S. Elliott, and D. L. Morton, "Normal tissue and solid tumor effects of hyperthermia in animal models and clinical trials," *Cancer Res.*, vol. 39, no. 6_Part_2, pp. 2245–2251, 1979.
[6] J. Hau, "Animal models for human diseases: An overview," in *Sourcebook of Models for Biomedical Research.* 2008, pp. 3–8.
[7] W. A. Weber, "Assessing tumor response to therapy," *J. Nucl. Med.*, vol. 50, no. Suppl 1, pp. 1S–10S, 2009.
[8] L. F. Bernabe et al., "Evaluation of the adverse event profile and pharmacodynamics of toceranib phosphate administered to dogs with solid tumors at doses below the maximum tolerated dose," *BMC Vet. Res.*, Springer, vol. 9, pp. 1–10, 2013, Art. no. 190.
[9] S. A. Geller and R. E. Horowitz, "Gross examination," in *Histopathology: Methods and Protocols*, S.A. Geller, Ed., New York, NY, USA: Springer, 2014, pp. 3–19.
[10] B. Mildenhall, P. P. Srinivasan, M. Tancik, J. T. Barron, R. Ramamoorthi, and R. Ng, "Nerf: Representing scenes as neural radiance fields for view synthesis," *Commun. ACM*, vol. 65, no. 1, pp. 99–106, 2021.
[11] A. Suvarna et al., "DeltaAI: Semi-autonomous tissue grossing measurements and recommendations using neural radiance fields for rapid, complete intraoperative histological assessment of tumor margins," 2023, *bioRxiv:2023.08.07.552349*.
[12] S. A. Goss, R. L. Johnston, and F. Dunn, "Comprehensive compilation of empirical ultrasonic properties of mammalian tissues," *J. Acoust. Soc. Am.*, vol. 64, no. 2, pp. 423–457, Sep. 1978.
[13] F. A. Duck, *Physical Properties of Tissue: A Comprehensive Reference Book*, London, U.K.: Academic Press, 1990.

[14] S. M. Hewitt et al., "Tissue handling and specimen preparation in surgical pathology issues concerning the recovery of nucleic acids from formalin-fixed, paraffin-embedded tissue," *Arch. Pathology Lab. Med.*, vol. 132, no. 12, pp. 1929–1935, 2008.
[15] S. K. Suvarna, "The gross room/surgical cut-up including sample handling," in *Bancroft's Theory and Practice of Histological Techniques*, 8th ed., S. K. Suvarna, C. Layton, and J. D. Bancroft, Eds., London, U.K.: Elsevier, pp. 64–72, 2019.
[16] DermaNet, "DermaNet All about the skin." Accessed: Feb. 20, 2025. [Online]. Available: https://dermnetnz.org/cme/lesions/processing-skin-biopsies
[17] D. Wolfe, "Tissue processing," in *Bancroft's Theory and Practice of Histological Techniques*, 8th ed. Elsevier, pp. 73–83, 2018.
[18] L. BioSystems, "Steps to better grossing guidelines." Accessed: Feb. 20, 2025. [Online]. Available: https://www.leicabiosystems.com/it-it/knowledge-pathway/steps-to-better-grossing/
[19] M. Tancik et al., "Nerfstudio: A modular framework for neural radiance field development," in *Proc. ACM SIGGRAPH Conf.*, 2023, pp. 1–12.
[20] C. Griwodz et al., "AliceVision Meshroom: An open-source 3D reconstruction pipeline," in *Proc. 12th ACM Multimedia Syst. Conf.*, 2021, pp. 241–247.
[21] J. L. Schonberger and J.-M. Frahm, "Structure-from-motion revisited," in *Proc. IEEE Conf. Comput. Vis. Pattern Recognit.*, 2016, pp. 4104–4113.
[22] H. Azhari, *Basics of Biomedical Ultrasound for Engineers.* Hoboken, NJ, USA: Wiley, 2010.
[23] "Intel® RealSenseTM product family D400 series datasheet." Accessed: Feb. 12, 2025. [Online]. Available: https://www.intel.com/content/www/us/en/content-details/841984/intel-realsense-d400-series-product-family-datasheet.html
[24] J. Gamper, N. Alemi Koohbanani, K. Benet, A. Khuram, and N. Rajpoot, "PanNuke: An open pan-cancer histology dataset for nuclei instance segmentation and classification," in *Proc. 15th Eur. Congress Digital Pathol., ECDP*, 2019, pp. 11–19.
[25] N. Brancati et al., "BRACS: A dataset for breast carcinoma subtyping in H&E histology images," *Database*, vol. 2022, 2022, Art. no. baac093.
[26] W. Hu et al., "GasHisSDB: A new gastric histopathology image dataset for computer aided diagnosis of gastric cancer," *Comput. Biol. Med.*, vol. 142, 2022, Art. no. 105207.
[27] F. Wilm et al., "Pan-tumor canine cutaneous cancer histology (catch) dataset," *Sci. Data*, vol. 9, no. 1, 2022, Art. no. 588.
[28] M. K. K. Niazi, A. V. Parwani, and M. N. Gurcan, "Digital pathology and artificial intelligence," *Lancet Oncol.*, vol. 20, no. 5, pp. e253–e261, May 2019.
[29] M. B. Lemos and E. Okoye, *Atlas of Surgical Pathology Grossing*, Cham, Switzerland: Springer, 2019.
[30] O. Eminaga et al., "Critical evaluation of artificial intelligence as a digital twin of pathologists for prostate cancer pathology," *Sci. Rep.*, vol. 14, no. 1, 2024, Art. no. 5284.
[31] J.-K. Kim, S.-J. Lee, S.-H. Hong, and I.-Y. Choi, "Machine-learning-based digital twin system for predicting the progression of prostate cancer," *Appl. Sci.*, vol. 12, no. 16, 2022, Art. no. 8156.
[32] Y. Tew, W. Y. Lee, and G. M. Tam, "Parallel Computing Using CUDA and MultiThreading in Background Removal Process," in *Proc. 3rd Int. Conf. Digit. Transformation IEEE Int. Symp. Spread Spectr. Tech. Appl. (ICDXA)*, 2024, pp. 237–242.